

**Understanding phase-change materials with unexpectedly low resistance drift
for Phase-change memories**

Chao Li^a, Chaoquan Hu^{a*}, Jianbo Wang^b, Xiao Yu^a, Zhongbo Yang^a, Jian Liu^a,
Yuankai Li^a, Chaobin Bi^a, Xilin Zhou^{c*} and Weitao Zheng^{a, d*}

^a *State Key Laboratory of Superhard Materials, Key Laboratory of Automobile
Materials of MOE, School of Materials Science and Engineering, Jilin University,
Changchun 130012, China*

E-mail: cqhu@jlu.edu.cn; wzcheng@jlu.edu.cn

^b *School of Science, Changchun University of Science and Technology, Changchun
130022, China*

^c *Max Planck Institute of Microstructure Physics, Weinberg 2, D-06120, Halle (Saale),
Germany*

E-mail: xilin.zhou@mpi-halle.mpg.de

^d *State Key Laboratory of Automotive Simulation and Control, Jilin University,
Changchun 130025, China*

This file includes:

Figures S1-S13

References 1-5

Section I The influence of annealing on the surface morphologies and the phase transitions of films

The AFM images of films with different vacancies and nitrogen concentrations before and after annealing are showed in Figure S1 and S2. Figure S1 demonstrates that all films are smooth with homogeneous surfaces. The same phenomenon is also observed in nitrogen-doped films. There is no obvious change of the surface morphologies of all films after annealing, which indicated that annealing at 50 °C did not significantly affect the surface morphologies of the films.

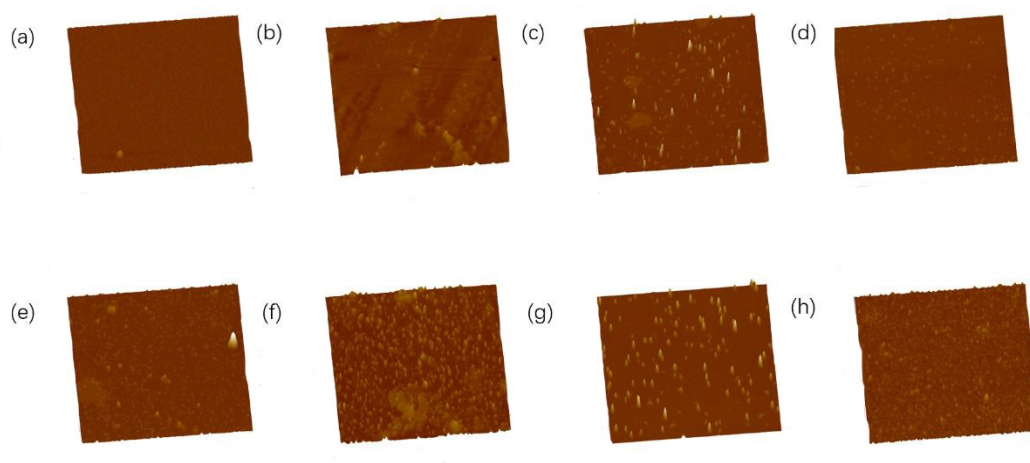


Figure S1 The AFM images of films with different vacancy concentration before and after annealing; The scan size is $5 \times 5 \mu\text{m}^2$. a-d are the morphologies of films with the vacancy concentration of 9.1, 20.0, 25.0, and 28.6% before annealing, respectively; e-h are the morphologies of films with the vacancy concentration of 9.1, 20.0, 25.0, and 28.6% after annealing, respectively.

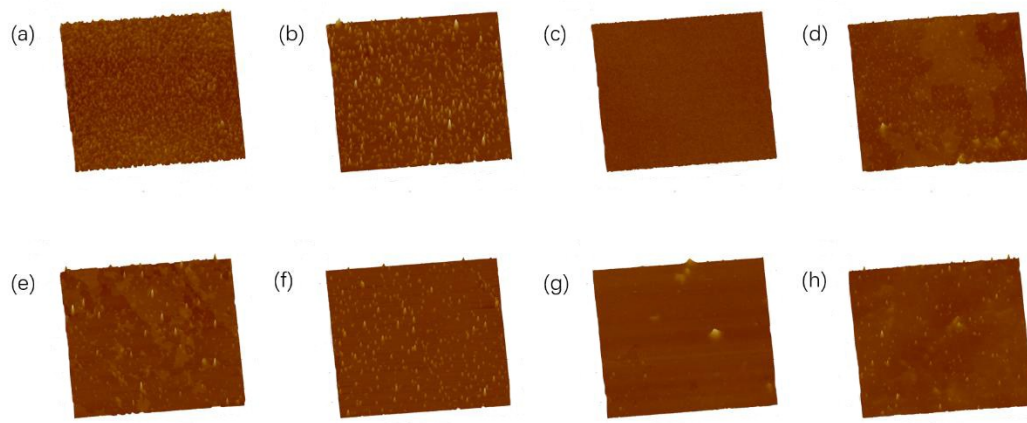


Figure S2 The AFM images of films with different nitrogen concentration before and after annealing; The scan size is $5 \times 5 \mu\text{m}^2$. a-d are the morphologies of films with the nitrogen concentration of 5.8, 10.0, 10.9, and 11.3 at.% before annealing, respectively; e-h are the morphologies of films with the vacancy concentration of 5.8, 10.0, 10.9, and 11.3 at.% after annealing, respectively.

Figure S3 and S4 show the SEM images of films with different vacancy and nitrogen concentration before and after annealing. It is clearly shown that the surfaces of all films are homogeneous and there is no significant change after annealing. This result is in agreement with AFM images and indicates that annealing did not affect the surface morphology of the film.

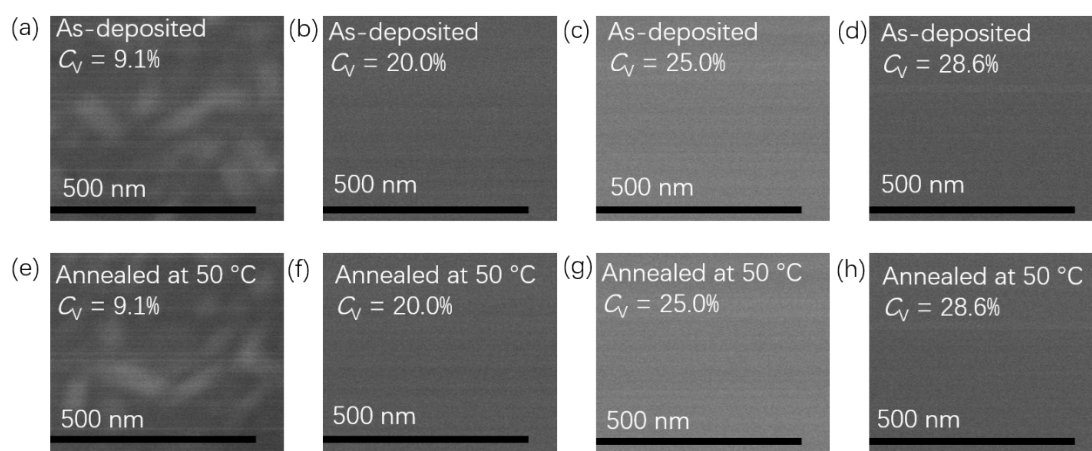


Figure S3 The SEM images of films with different vacancy concentration (C_V) before and after annealing. a-d are the morphologies of films with the vacancy concentration of 9.1, 20.0, 25.0, and 28.6% before annealing respectively; e-h are the morphologies of films with the vacancy concentration of 9.1, 20.0, 25.0, and 28.6% after annealing, respectively.

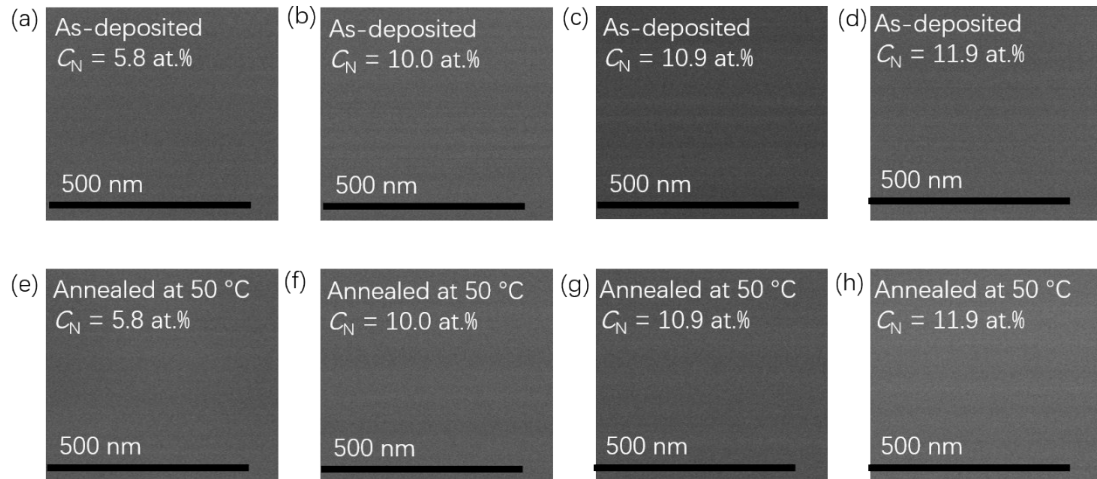


Figure S4 The SEM images of films with different nitrogen concentration (C_N) before and after annealing. a-d are the morphologies of films with the nitrogen concentration of 5.8, 10.0, 10.9, and 11.3 at.% before annealing, respectively; e-h are the morphologies of films with the vacancy concentration of 5.8, 10.0, 10.9, and 11.3 at.% after annealing, respectively.

Figure S5a and S5c show that there are no obvious crystallization peaks occur in all as-deposited films, which indicates that all films are amorphous. After annealing at 50 °C for 3h, there are still no obvious crystallization peaks appeared. Our XRD indicates that no phase transition occurred during the annealing and all films remained in the amorphous structure. The same phenomenon is observed in the Electron Diffraction as shown in Figure S6.

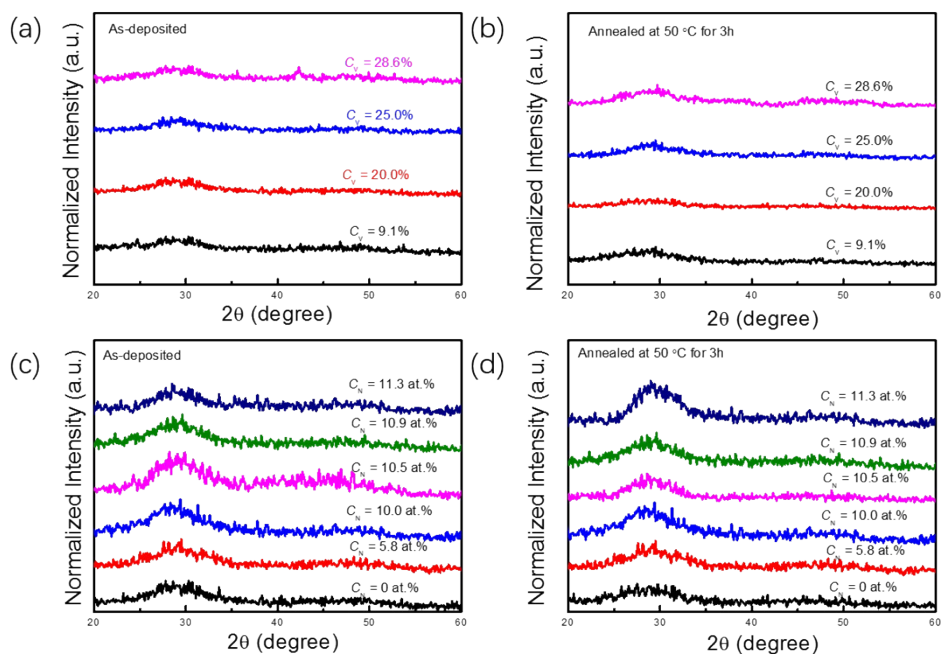


Figure S5 XRD of (a) as-deposited films with different vacancy concentration, (b) annealed at 50 °C, (c) as-deposited films with different nitrogen content and (d) annealed at 50 °C.

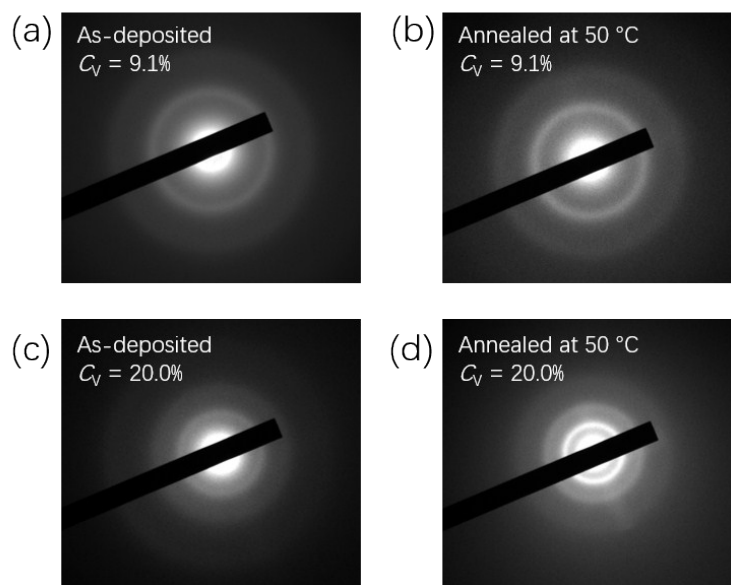


Figure S6 Electron Diffraction of (a) the as-deposited and (b) annealed films with $C_v = 9.1\%$, (c) the as-deposited and (d) annealed films with $C_v = 20.0\%$.

Section II The effect of vacancy on the rigidity of films

Figure S7 shows the hardness and elastic modulus of the films with different vacancy concentration. With the increase of vacancy concentration, the hardness and elastic modulus of the films first increased and then decreased. When the vacancy concentration was 20%, the hardness and elastic modulus reached the maximum value, which indicates that the rigidity of the film was the highest. This is in contrast to the trend of the resistance drift coefficient (Figure 2b in the main text). The result demonstrates that the higher rigidity, the lower resistance drift coefficient. Therefore, proper vacancy introduction will reduce the resistance drift caused by structural relaxation. It indicates that structural relaxation is difficult to occur in the film with higher rigidity owing to its more stable amorphous network. Therefore, the film with a vacancy concentration of 20% has the lowest resistance drift exponent.

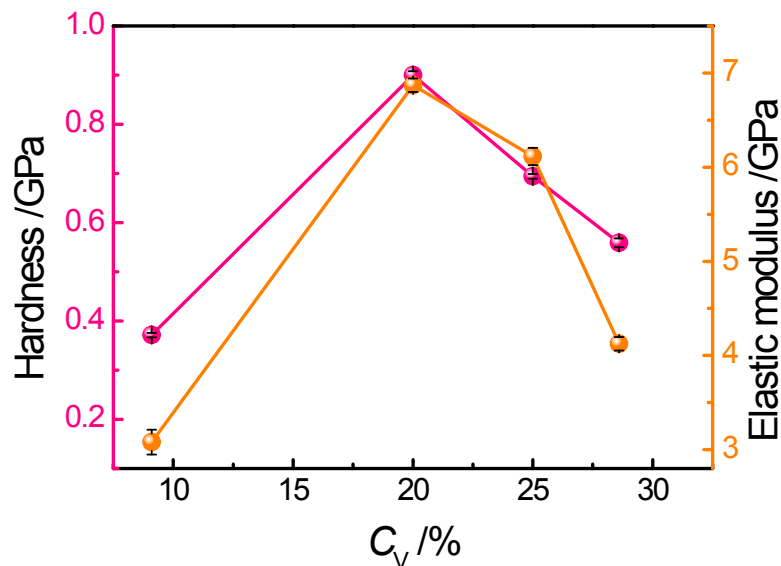


Figure S7 The hardness and elastic modulus of the films with different vacancy concentration.

Section III Results of XRD and SAED

Our XRD and SAED results show that the as-deposited nitrogen doped $\text{Ge}_2\text{Sb}_2\text{Te}_5$ films are amorphous. However, the films transform into a crystalline FCC structure after annealing at 250 °C as shown in Figure S8. A good periodic lattice can be clearly observed in Figures 3a and b.

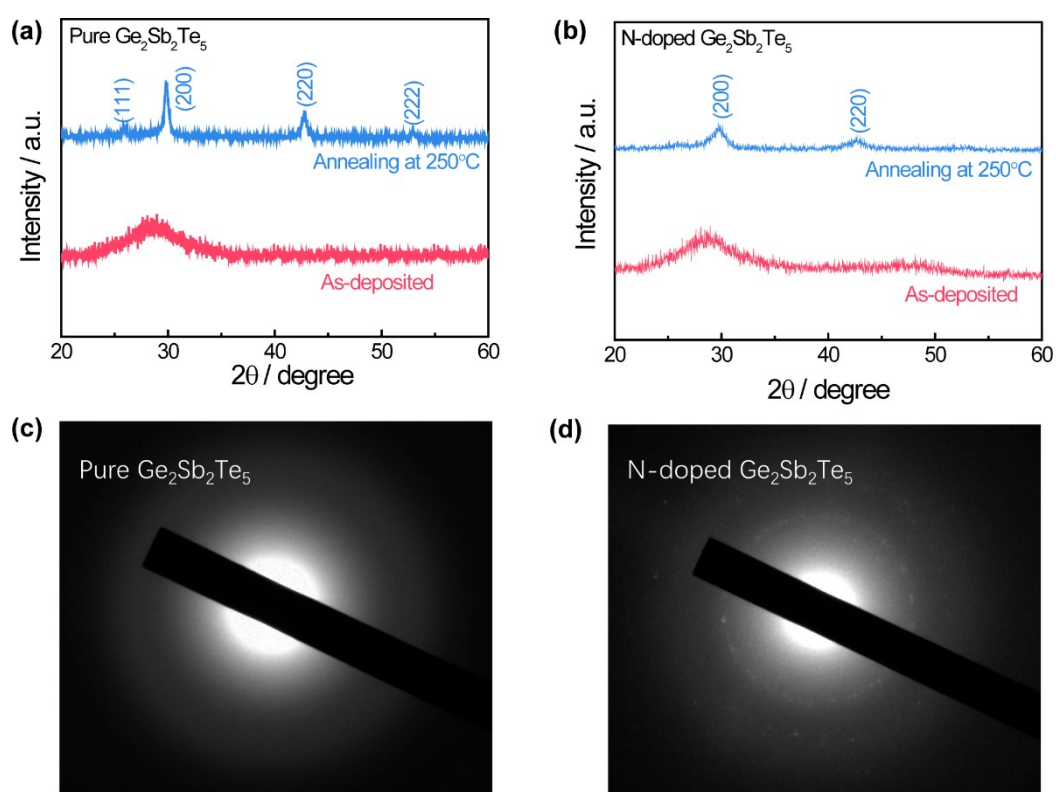


Figure S8 (a) The XRD of pure $\text{Ge}_2\text{Sb}_2\text{Te}_5$ films as-deposited and annealed at 250 °C. (b) The XRD of N-doped $\text{Ge}_2\text{Sb}_2\text{Te}_5$ films as-deposited and annealed at 250 °C. (c) The SAED of pure $\text{Ge}_2\text{Sb}_2\text{Te}_5$ films as-deposited. (d) The SAED of N-doped $\text{Ge}_2\text{Sb}_2\text{Te}_5$ films as-deposited.

Section IV Theoretical calculation

The models of $\text{Ge}_{13}\text{Sb}_{13}\text{Te}_{32}$ (Figure S9a) and $\text{N}_1\text{Ge}_{13}\text{Sb}_{13}\text{Te}_{32}$ (Figure S9b) were built by Materials Studio.^[4] The structure without nitrogen contains 58 atoms and the structure with nitrogen contains 59 atoms. The cutoff energy of geometric optimization was set to 205 eV and the k-point was set to $2 \times 2 \times 2$.

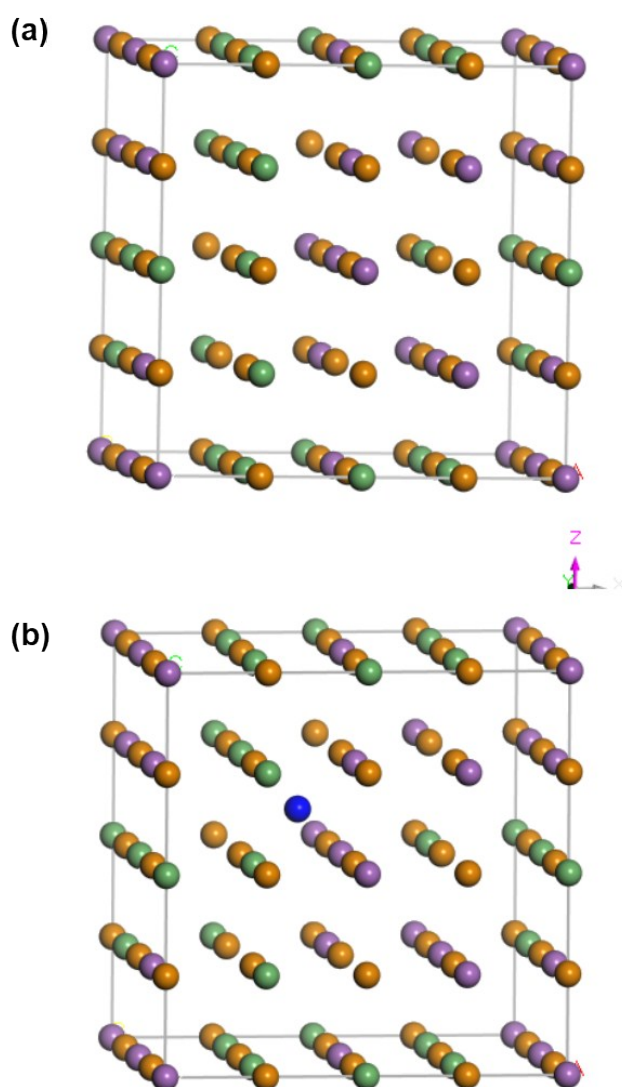


Figure S9 Models of $\text{Ge}_{13}\text{Sb}_{13}\text{Te}_{32}$ (a) and $\text{N}_1\text{Ge}_{13}\text{Sb}_{13}\text{Te}_{32}$ (b)

Section V Improvement of the storage properties

Comparison between the pure $\text{Ge}_2\text{Sb}_2\text{Te}_5$ ($C_N = 0$ at.%) and N- $\text{Ge}_2\text{Sb}_2\text{Te}_5$ ($C_N = 10.9$ at.%) films reveals that nitrogen doping enables a lower decreasing rate of intermediate resistance with annealing temperature and increases the temperature range for intermediate resistance state and the crystallization temperature.

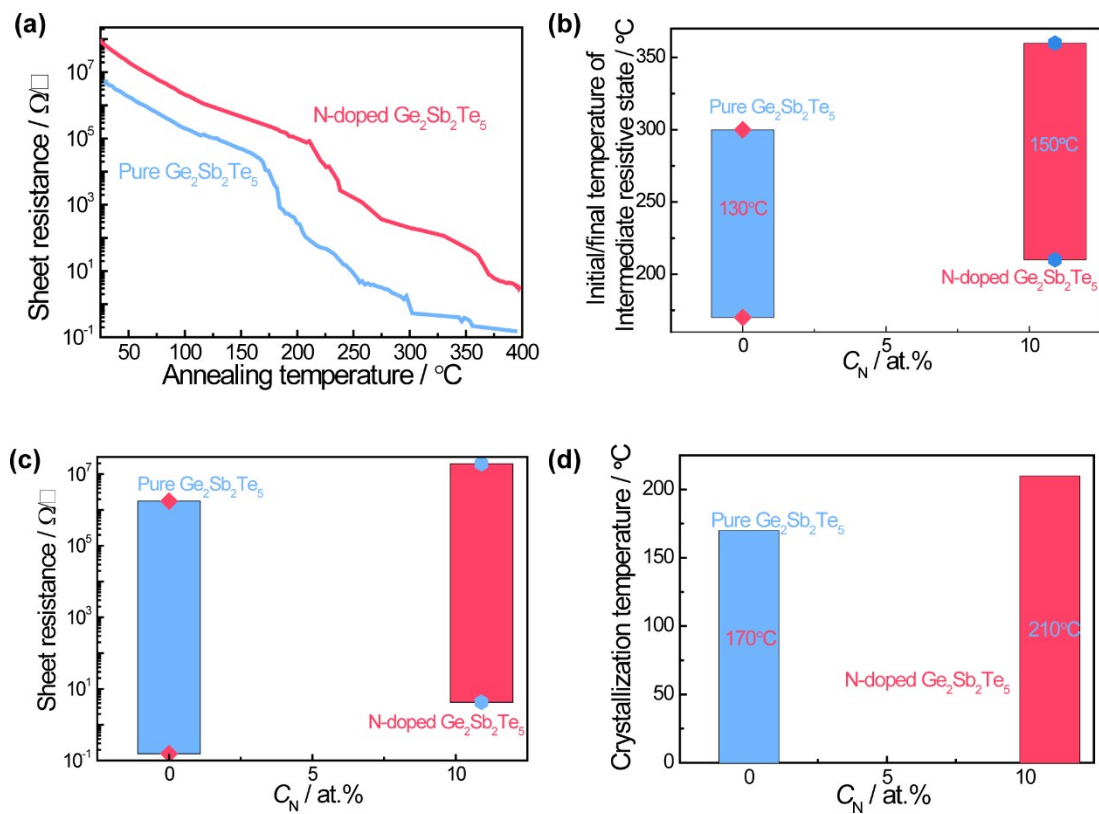


Figure S10 (a) The sheet resistance of pure and N-doped $\text{Ge}_2\text{Sb}_2\text{Te}_5$ films at different annealing temperature. (b) The initial/final temperature of intermediate resistance state of pure and N-doped $\text{Ge}_2\text{Sb}_2\text{Te}_5$ films. (c) The sheet resistance of amorphous and crystalline phases of pure and N-doped $\text{Ge}_2\text{Sb}_2\text{Te}_5$ films. (d) The crystallization temperature of pure and N-doped $\text{Ge}_2\text{Sb}_2\text{Te}_5$ films.

Section VI Device preparation

The steps of preparing T-shaped device cells are: (1) A W film (about 150 nm) was deposited on the Si substrate as the bottom electrode. (2) Positive photoresist with a thickness of about 1 μm was coated on the surface of W film. Using lift-off technology,^[1] we etched a series of small holes on the surface of the photoresist. The steps of photoetching are shown in Figure S11. (3) A SiO_2 film (about 600 nm) was deposited on the photoresist as an insulation layer after photoetching. (4) After removing the photoresist with acetone, a series of holes were formed in SiO_2 film. Then $\text{Ge}_2\text{Sb}_2\text{Te}_5$ ($C_N = 0\%$) and N- $\text{Ge}_2\text{Sb}_2\text{Te}_5$ ($C_N = 10.9\%$) films with a thickness of 750 nm were deposited on the samples, respectively. (5) Finally, a W film (about 150 nm) was deposited on the phase-change films as the top electrode. By this way, the devices based on pure $\text{Ge}_2\text{Sb}_2\text{Te}_5$ and N- $\text{Ge}_2\text{Sb}_2\text{Te}_5$ films were formed, respectively.

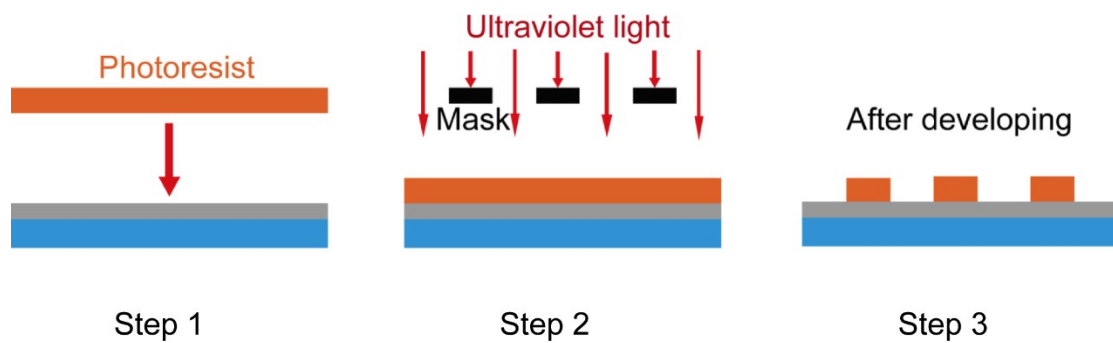


Figure S11 Steps of photoetching

Section VII Fitting of the refractive index and optical band gap by transmission spectroscopy

According to the envelope method,^[2] the refractive index of the weak absorption band (Figure S12a) can be obtained by the following formula:

$$n = \left[N + (N^2 - s)^{1/2} \right]^{1/2} \quad (1)$$

$$N = 2s \frac{T_M - T_m}{T_M T_m} + \frac{s^2 + 1}{2} \quad (2)$$

where s is the refractive index of substrate (For glass, it is 1.52), T_m and T_M represent the lower and upper transmittance, respectively, and n is the refractive index of the films.

The absorption coefficient α is calculated by the following formula:

$$\alpha = -\frac{1}{d} \ln \zeta \quad (3)$$

$$\zeta = \frac{C_1 \left[1 - (T_M / T_m)^{1/2} \right]}{C_2 \left[1 + (T_M / T_m)^{1/2} \right]} \quad (4)$$

$$C_1 = (n_0 + n)(n + s) \quad (5)$$

$$C_2 = (n_0 - n)(n - s) \quad (6)$$

where $n_0 = 1$, d is the film thickness, α is the absorption coefficient. The optical band gap is calculated by Tauc's method.^[3] As shown in Figure S12b, a straight line is fitted near the absorption limit. The optical band gap is obtained from the point at which the extension of the straight line and the horizontal axis intersect.

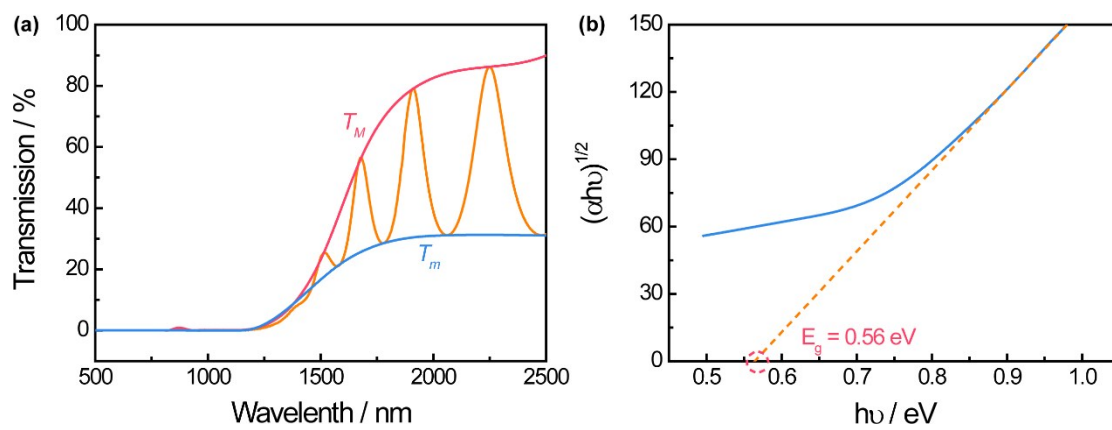


Figure S12 Lower and upper envelope (a) and fitting of optical band gap (b) by transmission spectroscopy

Section VIII The dependency relationship among resistance drift, band gap drift and the reciprocal drift of the dielectric coefficient

We defined the band gap drift exponent ν_E according to the expression of the resistance drift exponent. Figure S13a and d show the dependences of ν_R , ν_E and $\nu_{1/\epsilon}$ of films on vacancy concentration (C_V) and on doped nitrogen content (C_N), respectively. Clearly, they all decrease firstly and then increase. They reach the minimum value when $C_V = 20\%$ or $C_N = 10.9\%$. Figure S13b shows the linear relationship between ν_R and ν_E of films with different vacancy concentrations. Figure S13c shows the linear relationship between ν_E and $\nu_{1/\epsilon}$ of films with different vacancy concentrations. There is a proportional relationship among ν_R , ν_E and $\nu_{1/\epsilon}$. Similar trend is also observed for the films with different nitrogen contents (Figures S13e and f). The strong dependence of ν_R , ν_E and $\nu_{1/\epsilon}$ on vacancy concentration and nitrogen content indicates that resistance drift in phase-change films originates from the change in dielectric coefficient.

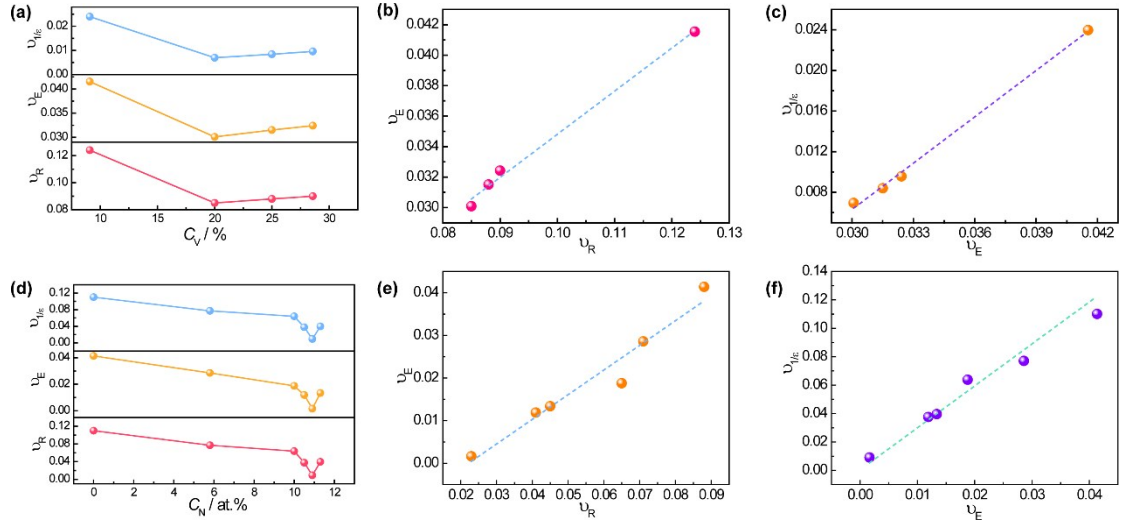


Figure S13 (a) The dependence of resistance drift v_R , band gap drift v_E and the reciprocal of the dielectric coefficient drift $v_{1/\epsilon}$ on vacancy concentration. (b) The linear relationship of v_R and $v_{1/\epsilon}$. (c), The linear relationship of v_E and $v_{1/\epsilon}$. (d), The dependence of v_R , v_E , and $v_{1/\epsilon}$ on doped nitrogen content. (e), The linear relationship of v_R and $v_{1/\epsilon}$. (f), The linear relationship of v_E and $v_{1/\epsilon}$.

Supplementary References

- [1] K. Lee, J. Lee, B. A. Mazor, S. R. Forrest, *Light: Sci. Appl.* **2015**, *4*, e288.
- [2] R. Swanepoel, *J. Phys. E: Sci. Instrum.* **1983**, *16*, 1214.
- [3] Z. Liu, F. Huang, H. Huang, S. Zhang, K. Zhang, W. Zheng, C. Hu, *Vacuum* **2017**, *141*, 32.
- [4] a) J. Hegedus, S. R. Elliott, *Nat. Mater.* **2008**, *7*, 399; b) J. Tominaga, A. V. Kolobov, P. Fons, T. Nakano, S. Murakami, *Adv. Mater. Interfaces* **2014**, *1*, 1300027.